BNL-213630-2020-JAAM

Out-of-plane magnetic anisotropy enhancement in La1-xSrxCoO3-delta/La2/3Sr1/3MnO3/La1-xSrxCoO3-delta thin films

W. Wang,

To be published in "PHYSICAL REVIEW B"

January 2020

Condensed Matter Physics and Materials Science Department

Brookhaven National Laboratory

U.S. Department of Energy

USDOE Office of Science (SC), Basic Energy Sciences (BES) (SC-22)

DISCLAIMER

Out-of-plane magnetic anisotropy enhancement in $La_{1-x}Sr_xCoO_{3-\delta}/La_{2/3}Sr_{1/3}MnO_3/La_{1-x}Sr_xCoO_{3-\delta}$ thin films

Wei Wang[1,2,3], Jine Zhang[1,2], Xi Shen[1], Xiangxiang Guan[1,2], Yuan Yao[1], Junjie Li[1], Changzhi Gu[1,2], Jirong Sun[1,2], Yimei Zhu[3], Jing Tao[3,*], Richeng Yu[1,2,*]

1. Beijing National Laboratory of Condensed Matter Physics, Institute of Physics, Chinese Academy of Sciences, Beijing 100190, P. R. China.

2. School of Physical Sciences, University of Chinese Academy of Sciences, Beijing 100049, P.R. China.

3. Condensed Matter Physics and Materials Science Division, Brookhaven National Laboratory, Upton, New York 11973, USA

*Corresponding authors: rcyu@iphy.ac.cn; jtao@bnl.gov

ABSTRACT

Perpendicular magnetic anisotropy (PMA) in multilayer thin films promotes the development of spintronic and magnonic research fields. The origin of the PMA deserves a thorough investigation since it contains rich physics related to multiple factors in the heterostructure system. Here, we study the origin of PMA in $La_{2/3}Sr_{1/3}MnO_3$ (LSMO) thin films sandwiched by $La_{1-x}Sr_xCoO_{3-\delta}$ (LSCO) layers grown on $SrTiO_3$ substrate, using aberration-corrected scanning transmission electron microscopy. Our findings indicate that the lattice and electronic structures of LSMO can be modified through the inhomogeneous strains induced by nanodomains in LSCO layers. Moreover, we infer that the lattice distortion in LSCO at low

temperatures is a driving force to reorient the spin moment from in-plane direction to out-of-plane direction in LSMO, which could be the nature of the PMA formation. The symmetry breaking in the LSMO layer induced by the domains from LSCO enhances magnetic anisotropy energy in LSMO.

I. INTRODUCTION

The novel physical properties of strongly electron correlated oxides are thought to be a consequence of the intricate interplay among charge, spin and orbital degrees of freedom, for example, Mott insulators, metal-insulator transitions, multiferroics, superconductivity, etc. [1]. In recent years, there has been a burst of activity to manipulate these phenomena using oxide heterostructures by tuning the interactions between charge, spin, orbital, and lattice [2-4].

Manganites have been accepted to be a popular system for the study of strongly correlated electron system oxides for their abundant electronic phases [5, 6]. For example, bulk $La_{2/3}Sr_{1/3}MnO_3$ (LSMO) with half-metallic character has nearly 100% spin polarization of the conduction electron [7], which makes LSMO a promising material candidate for the fabrication of magnetic tunnel junctions, sensors and spintronic devices [8-10]. For LSMO thin films, interface strain, film thickness, and chemical doping are shown to have important effects on tailoring the physical properties, specifically the magnetic properties, such as magnetic anisotropy [11-14]. Furthermore, perpendicular magnetic anisotropy (PMA) in the multilayers films is currently of great technological interest, for example, in the magnetic and

magneto-optical storage media [15, 16]. Therefore, the ability to stabilize the PMA and understanding the PMA mechanisms are important both experimentally and theoretically [17-19].

In a two-dimensional thin-film system, PMA originating from an intrinsic anisotropy mechanism is strong enough to overcome the extrinsic macroscopic shape anisotropy, which prefers in-plane magnetic orientation [20]. The underlying physics of the PMA is still far from being fully understood, despite intensive experimental and theoretical studies, which have proposed different explanations for the PMA in some ultrathin films and multilayers. One possible interpretation of the PMA mechanism is based on lattice symmetry breaking and the asymmetric bonding at the surface and interfaces due to the lattice mismatch strains [21, 22]. Some studies have suggested that the interfacial hybridization via enhanced orbital moment causes the PMA in multilayers. Therefore, it is believed that the magnetocrystalline anisotropy (MCA) is based on the preferred direction of the orbital moment [23, 24]. In addition, it is also suggested that spin reorientation transition is linked to the change in MCA [16].

To further explore the physical origin of PMA, we demonstrate a PMA enhancement in a LSMO layer sandwiched by two $La_{1-x}Sr_xCoO_{3-\delta}$ (LSCO) films. Due to the interface effects, a relatively low Curie temperature (T_c) and the degradation of magnetic properties would be induced in LSMO thin films [25-27]. In order to eliminate these degraded effects and avoid structure defects, we prepared LSMO thin films with trilayer structures instead of a multiple layers structure. We found that the magnetic anisotropy energy (MAE) is increased by two orders of magnitude

compared with that in the LSMO bulk and the T_c is at room temperature (RT).

Different from LSMO, LSCO thin films have attracted much attention due to modulated dark stripes in the lattice structures, the origin of which is still in heated debate [28-31]. Using aberration-corrected scanning transmission electron microscopy (STEM), we observed that there are modulated stripes in LSCO grown on $SrTiO_3$ (STO) substrate. The dark-stripe superstructures are highly oxygen deficient and the dark stripes with different orientations can be treated as nanodomains. These nanodomains play a critical role in providing inhomogeneous external strains to the LSMO film, which possibly results in tuning the magnetic properties of the LSMO film. However, when the trilayer is grown on $LaAlO_3$ substrate, the dark stripe structure is absent [32]. These experimental observations demonstrate that the dark stripe formation in LSCO probably depends on external strains. In addition, we observed the changes of electronic structures of LSCO and LSMO at low temperatures using electron energy-loss spectroscopy (EELS). Based on the experimental observation reported by Rui and Klie. [33], we infer that there is more MnO_6 octahedra elongation along the *c* axis in LSMO induced by the reduced lattice spacing of LSCO at low temperatures. The crystal structure distortion in LSMO gives rise to a $d_{3z^2-r^2}$ orbital preferential occupancy. Considering the spin-orbit interaction in transition metals [23], the "out-of-plane" orbitals redirect spin moment from in-plane to out-of-plane direction and further generates PMA in the LSMO film.

II. EXPERIMENTAL DEAILS

Two thin films with a LSCO/LSMO/LSCO (x = 0.2 and 0.5) sandwiched structure were grown on (001)-orientated STO substrate by the pulsed laser ablation technique. The layer thicknesses of LSCO (nominal 7 nm) and LSMO (nominal 5 nm) were fixed in the two samples. The samples for the TEM experiments were prepared in two methods: by mechanical polishing followed by an Ar ion milling in the temperature of liquid nitrogen and by focused ion beam. STEM and EELS studies were carried out on a JEOL-ARM 200F with double Cs correctors. The lattice structures of the sample were acquired in atomic resolution high-angle annular dark-field (HAADF) images and annular bright-field (ABF) images.

III. RESULTS AND DISCUSSION

A. Microstructures of the thin films

Figures 1(a) and 1(c) show cross-sectional HAADF images of the two thin films. There are some ordered dark stripes presented in the $La_{0.8}Sr_{0.2}CoO_{3-\delta}$ and $La_{0.5}Sr_{0.5}CoO_{3-\delta}$ layers. According to the occurrence of dark stripes in the $La_{0.8}Sr_{0.2}CoO_{3-\delta}$ layers in Fig. 1(a), the periodicities in dark stripes are close to $3a_p$ and $2a_p$, whereas only the $2a_p$ -modulated dark stripes are found in the $La_{0.5}Sr_{0.5}CoO_{3-\delta}$ layers (Fig. 1(c)), where a_p is the pseudocubic lattice constant of STO. The directions of the dark stripes are either parallel (horizontal) or perpendicular (vertical) to the interface. The strong diffraction spots in the electron diffraction patterns in Figs. 1(b) and (d) come from STO substrate. The split diffraction spots marked by two circles in the rectangle in Fig. 1(b) indicate that the lattice parameters of the film are larger than

those of STO substrate. Considering that the lattice parameter of bulk LSMO (3.87 Å) is smaller than that of bulk STO (3.905 Å) [34, 35], this result seems to be unreasonable without the consideration of the LSCO film, the structures of which are characterized in the next section. Surprisingly, these mixed modulated structures ($2a_p$ and $3a_p$) in LSCO/LSMO/LSCO with the Sr doping level x = 0.2 result in weak streaks in the selected area electron diffraction pattern in Fig. 1(b). In contrast, discrete reflections that are corresponding to an approximate periodicity of $2a_p$ in the LSCO/LSMO/LSCO with x = 0.5 film can be seen in Fig. 1(d).

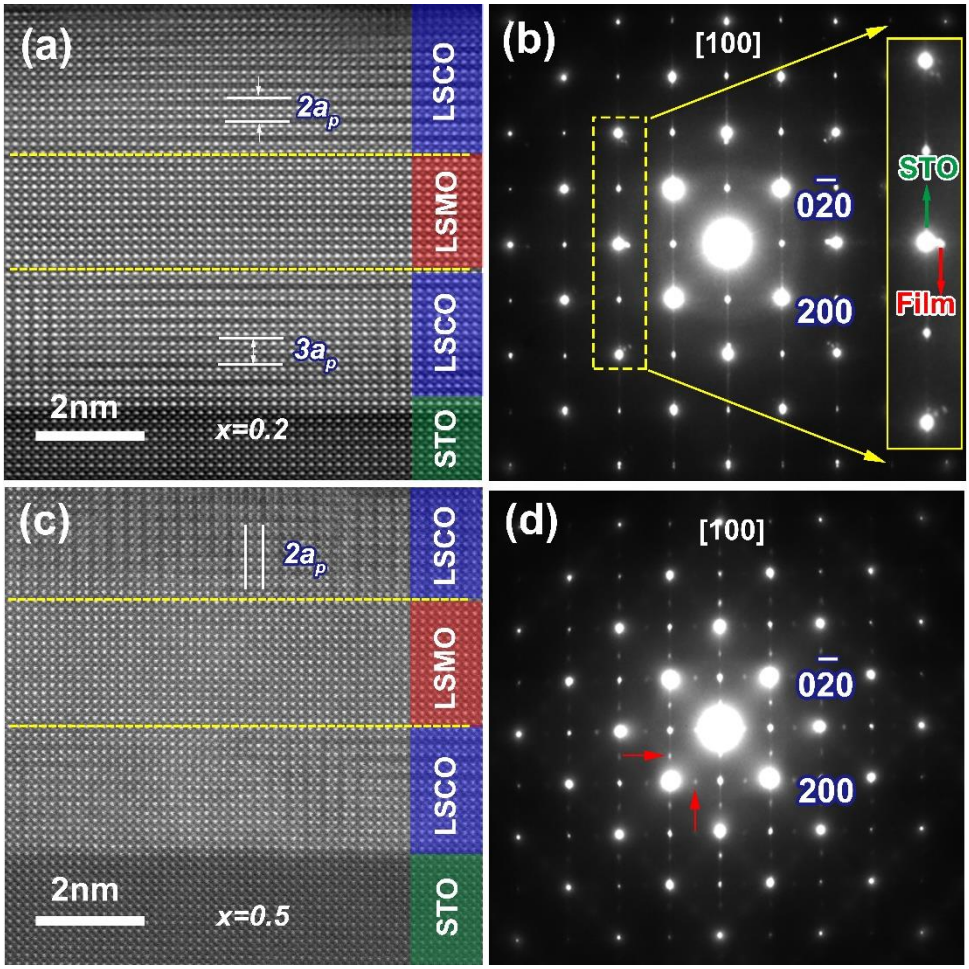

FIG. 1. (a) and (c) Cross sectional HAADF images of LSCO/LSMO/LSCO-STO thin films (doping level of Sr (x) = 0.2 and 0.5, respectively). The yellow dashed lines are

the LSCO/LSMO interfaces. (b) and (d) Corresponding SAED patterns including the contributions of both the film and substrate along the [100] zone axis. The inset in (b) is an enlarged view from the region marked by the yellow rectangle. It can be seen that there are two sets of reflections from the STO substrate (red arrow) and from the LSMO/LSCO film (green arrow). The reflections marked by red arrows in (d) are the superlattice reflections from LSCO (x = 0.5) with a $2a_p$ periodicity (dark stripes).

B. Crystal structures of $La_{0.8}Sr_{0.2}CoO_{3-\delta}$ and $La_{0.5}Sr_{0.5}CoO_{3-\delta}$

Since the magnetic anisotropy of LSMO can be tuned by adjacent LSCO layers, it is necessary to figure out the microstructures of the modulated structures in LSCO films. The HAADF-STEM images with $3a_p$ and $2a_p$ periodicities for the dark stripes along the $[110]_p$ and $[1\bar{1}0]_p$ orientations are shown in Figs. 2(a)-2(d), respectively. In the HAADF images, the intensity of the atomic column is approximately proportional to $Z^{1.7}$, where Z is the atomic number [36]. The dark stripes with lower intensity compared with that of the bright stripes contribute to an increase of La-La distance around the dimmer plane of Co. Through the intensities of line profiles for Co atomic layers, the Co ion arrangement in the dark stripes can be seen. From the images along the $[110]_p$ zone axis in Figs. 2(a) and 2(c), it is visible that in the dark stripes every two Co ions form a pair (blue line profiles), which is called the breathing mode [37, 38]. This mode is present only in the $[110]_p$ direction, while along the $[1\bar{1}0]_p$ zone axis, the breathing mode is absent in the dark stripes, that is, the distance between Co ions is equal in the dark stripes. (See the yellow line profiles in Figs. 2(b) and (d)). These crystal structures mentioned above are consistent with the fingerprint of a

well-known brownmillerite structure (see Ref. [34] and crystal models in Figs. 2(e) and (f)).

To further identify the modulated structure in LSCO, we simulated HAADF images using crystal structure models of $La_2Co_2O_5$ and $La_3Co_3O_8$. The crystal structure of $La_2Co_2O_5$ is a typical brownmillerite structure composed of alternatively stacked CoO_6 octahedra and CoO_4 tetrahedra along the *c* axis [39, 40]. Meanwhile, $La_3Co_3O_8$ is an intermediate state between the brownmillerite and the perovskite structures. In our case, the structural characteristics in LSCO with $2a_p$ and $3a_p$ periodicities coincide with $La_2Co_2O_5$ and $La_3Co_3O_8$ crystal structures, respectively. Hence, the structure models for the HAADF image simulations in Figs. 2(a)-(d), are based on the $La_2Co_2O_5$ and $La_3Co_3O_8$ crystal structures.

The well-matched simulated images and the corresponding crystal structure models are inserted in Figs. 2(a)-(d). Figs. 2(a) and 2(b) are the intermediate structure in the $La_{0.8}Sr_{0.2}CoO_{3-\delta}$ thin films, and Figs. 2(c) and 2(d) are the brownmillerite structure in the $La_{0.5}Sr_{0.5}CoO_{3-\delta}$ thin films. Since ABF images are very sensitive to the light atoms (such as oxygen) compared with HAADF images, we observed the oxygen positions along the $[110]_p$ zone axis in Fig. 3(a). The oxygen atom arrangement coincides with the brownmillerite structure. According to the $La_2Co_2O_5$ crystal structure in Ref. [33], we find that the lattice parameter of the $La_2Co_2O_5$ is larger than that of STO. This may be the reason why the lattice parameter of the LSCO/LSMO/LSCO film is larger than that of STO substrate, as we have mentioned in Fig. 1(b).

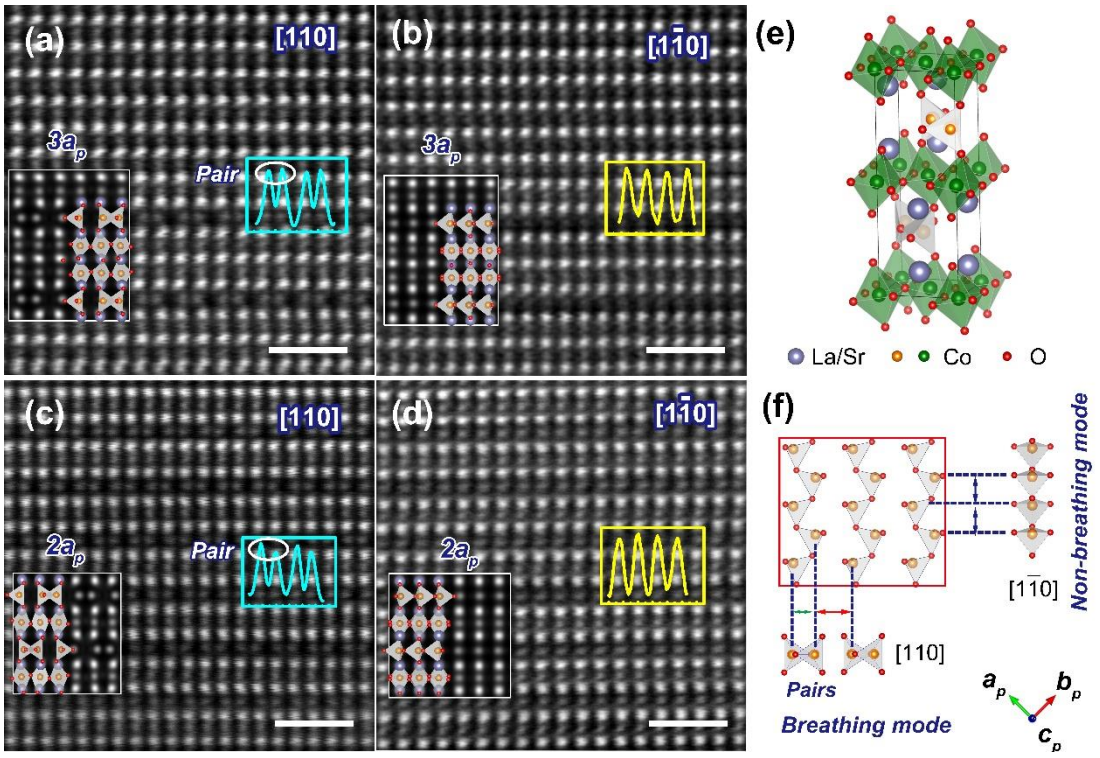

FIG. 2. (a) and (b) HAADF images with $3a_p$ periodic structure in LSCO along the $[110]_p$ and $[1\bar{1}0]_p$ zone axes. (c) and (d) HAADF images with $2a_p$ periodic structure in LSCO along the $[110]_p$ and $[1\bar{1}0]_p$ zone axes. The corresponding simulated HAADF images and crystal structure models are inserted. The scale bar in (a)-(d) is 1 nm. The inserted plots colored by blue and yellow lines are the line profiles of Co atoms in dark stripes. The blue one indicates every two Co atoms make pairs, the Co-Co distance in the yellow one is equally distributed. (e) A typical brownmillerite crystal structure. The blue sphere and red sphere are La/Sr and oxygen atoms, respectively, the orange and green spheres present Co ions in tetrahedron and octahedron, respectively. (f) An extracted CoO_4 tetrahedra layers in the dark stripes. The arrangements of Co ions along $[110]_p$ and $[1\bar{1}0]_p$ zone axes are shown. They are breathing mode and non-breathing mode, respectively.

C. Electronic structure of the dark stripe in LSCO

To shed light on the electronic structure of LSCO, EELS linescan was performed in the dark stripe and bright stripe in LSCO. Figs. 3(b) and 3(c) show the results of EELS Co $L_{3,2}$ and O K peaks in the dark stripe and the bright stripe, respectively. The Co L near-edge structure is very sensitive to the valence state of Co ions, the prepeak of the O K edge (peak a) is associated with the hybridization of O 2p with Co 3d orbitals, whereas peaks b and c can be attributed to the bonding strength of O 2p with La 5d and Co 4sp [41], respectively. In our experiments, the Co $L_{3,2}$ peaks in the dark stripe shift about 0.4 eV toward the lower energy side in the spectrum and the L_3/L_2 ratio in the dark stripe is higher than that in bright stripe. These results suggest that the valence of the Co ion in the dark stripe is lower than that in the bright stripe [42]. The corresponding fitting spectra of Co-$L_{3,2}$ peaks are presented in Supplemental Material Fig. S1 [43]. Moreover, the intensities of O K prepeak a and peak c in the dark stripe are also decreased compared with that in the bright stripe. Based on the EELS measurements, we conclude that the formation of the dark stripe is induced by oxygen deficiency. Furthermore, the existence of oxygen vacancy in the LSCO provides much more space for the atom displacements. Under external strains, the crystal structure of LSCO can be more easily modified via the formation of nanodomains, which will be explained in detail below.

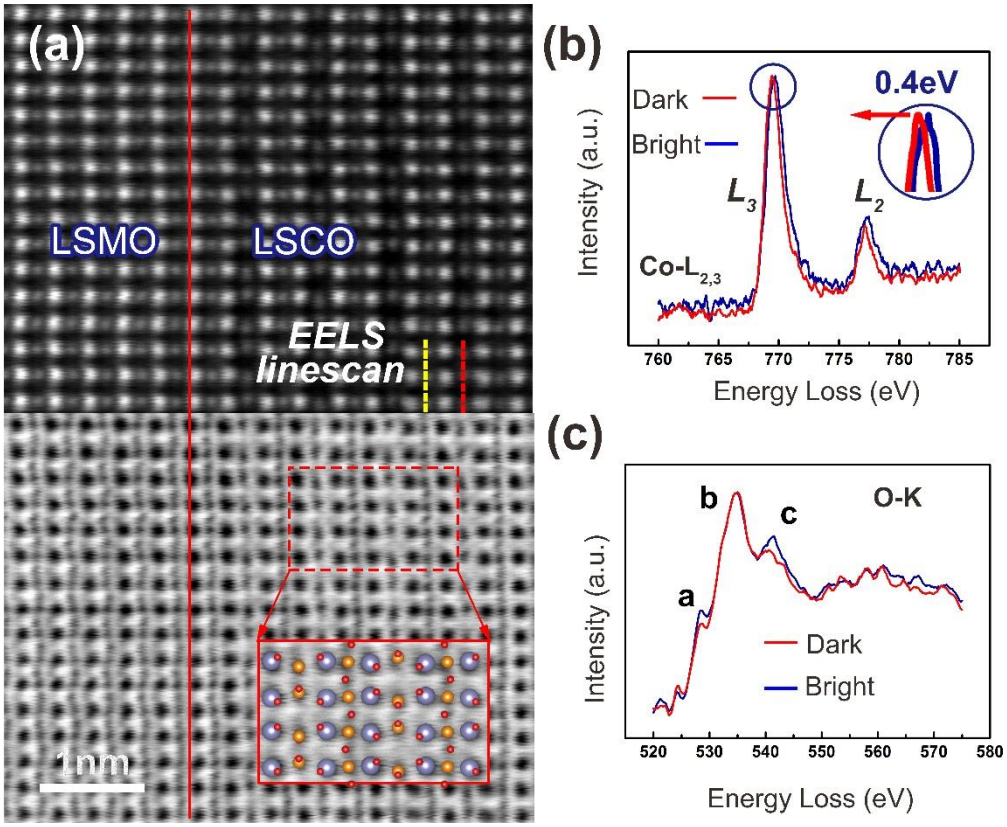

FIG. 3. (a) HAADF (up panel) and ABF (bottom panel) images with breathing mode in LSCO layer along the $[110]_p$ zone axis. Insert is the brownmillerite structure model, which is consistent with the extracted ABF image. The dashed lines in the HAADF image present the EELS linescan positions. (b) and (c) EELS spectra of Co-$L_{2,3}$ and O-K edges taken from the dark and bright stripes in LSCO in (a), respectively. The peak intensities in these spectra are normalized with L_3 peak and peak b in (b) and (c), respectively. The enlarged peaks in (b) show the energy loss for Co $L_{3,2}$ peaks in dark stripes shifts about 0.4 eV to the left side.

D. Nanodomains in the LSCO film due to brownmillerite structure

As shown in Fig. 4(a), horizontal and vertical dark stripes (in areas marked by the blue and red frames) coexist in LSCO along the [100] zone axis. According to the

characteristic of brownmillerite structure, these dark stripes with different orientations can be ascribed to different nanodomains with orthogonal brownmillerite structure in LSCO films: vertical dark stripes (left panel in Fig. 4(a) with the c_p axis parallel to the interface plane) and horizontal dark stripes (right panel in Fig. 4(a) with the c_p axis perpendicular to the interface plane). These two types of nanodomains can be formed through a 90° rotation around the b_p axis. Besides the changes in the orientation of the dark stripes, the breathing mode and nonbreathing mode in the dark stripes can be observed simultaneously along one zone axis ($[110]_p$ or/and $[1\bar{1}0]_p$), which is shown in Fig. 4(b). It indicates that the nanodomains of the LSCO layers can also rotate around the c_p axis. These different types of nanodomains in LSCO will cause inhomogeneous strains and thus different orbital orderings in LSMO.

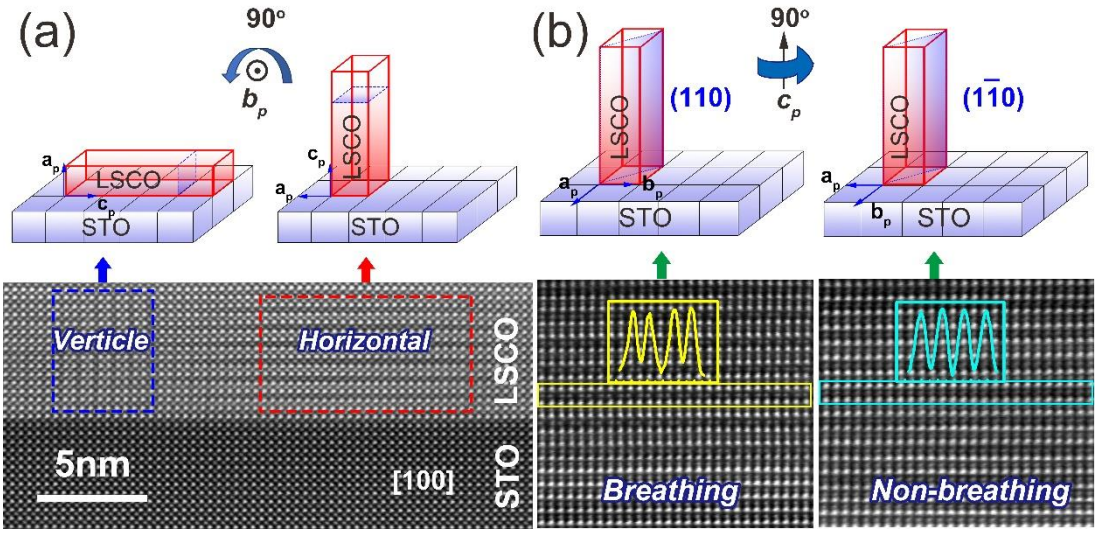

FIG. 4. (a) HAADF image with horizontal and vertical dark stripes marked by red and blue dashed rectangles in LSCO layer. Top half is structure models of domains: two 90° nanodomains with vertical and horizontal dark stripes around b_p axis of LSCO. Blue planes inserted in the models show the directions of dark stripes. (b) HAADF images with dark stripes resulted from breathing mode (marked by the yellow frame)

and without seeing breathing mode (non-breathing mode) in dark stripes (marked by the yellow frame) along one zone axis. Top half is structure models of domains: two 90° nanodomains around c_p axis of LSCO. The shadow planes indicate $(1\bar{1}0)$ and (110) planes of LSCO. The inserted plots colored by yellow and blue lines are the line profiles of Co atoms in dark stripes.

IV. Magnetic properties

The previous report in Ref. 11 pointed out that MAC of LSMO is closely related to the external strains. When LSMO thin film grows on LAO substrate, which provides in-plane compressive strain, the magnetic easy axis of LSMO is along the out-of-plane direction. Meanwhile, when LSMO grows on STO substrate with in-plane tensile strain, the corresponding magnetic easy axis is in the in-plane direction.

To further confirm the strain effects from LSCO to LSMO, we measured the lattice spacing along *a* and *c* axes in LSMO based on the HAADF images when either horizontal or vertical dark stripes are present in LSCO (Figs. 5(a) and 5(b)) as a comparison between the two areas (nanodomains). The measured results manifest that the horizontal dark stripes existing in the LSCO could provide an in-plane compressive stain to LSMO. Consequently, the *c/a* ratio >1 is partially present in LSMO layers, which indicates that the $d_{3z^2-r^2}$ orbital is preferentially occupied. However, the LSMO layer is in an in-plane tensile strained state when it is sandwiched by the LSCO with vertical dark stripes. In this case, the *c/a* ratio is less

than 1 (see Fig. 5(b)), i.e., e_g electrons are more likely to occupy the $d_{x^2-y^2}$ orbital [44-46]. Our measurement indicates that nanodomains in LSCO provide tensile or compressive strains in different regions at RT. Therefore, these mixed strains result in different lattice distortions, disordered orbital occupancy and different MAC in the different local regions of LSMO at RT.

Figure 5(c) shows the field cooling (FC) M-T curves of the film at x = 0.5. The film at x = 0.2 exhibits a similar magnetic behavior (see Supplemental Material Fig. S2 [43]). From the M-T curves, it can be concluded that the magnetic phase in LSMO is the FM phase and the magnetic easy axis is in the out-of-plane direction at low temperatures [47]. To figure out the mechanism of the PMA, we performed STEM-EELS measurements of O *K* edge at low temperature and compared with the EELS results at RT (shown in Fig. 5(d)). In the spectra at different temperatures, the changes from the intensities and the shapes of these peaks (marked by numbers 1 and 2) are evident in both LSCO and LSMO layers. As we have mentioned above, these peaks in O K edge correspond to Co-O/Mn-O bonding states. The changes in the O *K* edge may be related to the lattice distortions in LSCO/LSMO at low temperatures.

Moreover, Rui and Klie reported that the lattice spacings in the stripe phase of LSCO at low temperature are different from that at 300K [33]. The lattice spacing of the bright layer (i.e., La-La distance in the bright stripes) is reduced from 3.61Å (300K) to 3.51 Å (95K). The lattice spacing of the dark layer (i.e., La-La distance in the dark stripes) is enlarged from 4.29 Å (300K) to 4.33 Å (95K). The variation of lattice spacing may be the reason for the peak changes in EELS spectra in Fig. 5(d).

Though both expansion and contraction of the lattice spacing occur in the same dark stripe phase, considering that the reduced lattice spacing (~0.1 Å) in the bright stripes is larger than the enlarged lattice spacing (~0.04 Å) in the dark stripes, the total effect is a contraction of the in-plane lattice parameters at low temperatures. That is, LSCO layers with vertical stripes gradually provide compressive strain, instead of tensile strain, to the LSMO layer as the temperature decreases. Under the in-plane compressive strain at low temperatures, more MnO_6 octahedra are elongated along the *c* axis, and the $d_{3z^2-r^2}$ orbital is preferentially occupied in LSMO. Due to the bonding anisotropy in the lattice, the orbital moment will redirect the spin moment into a favorable lattice direction, i.e. *c* axis, given the spin-orbit coupling in transition metals [48, 49]. Hence, the total magnetic moment is in the out-of-plane direction at low temperature in our samples [50-52].

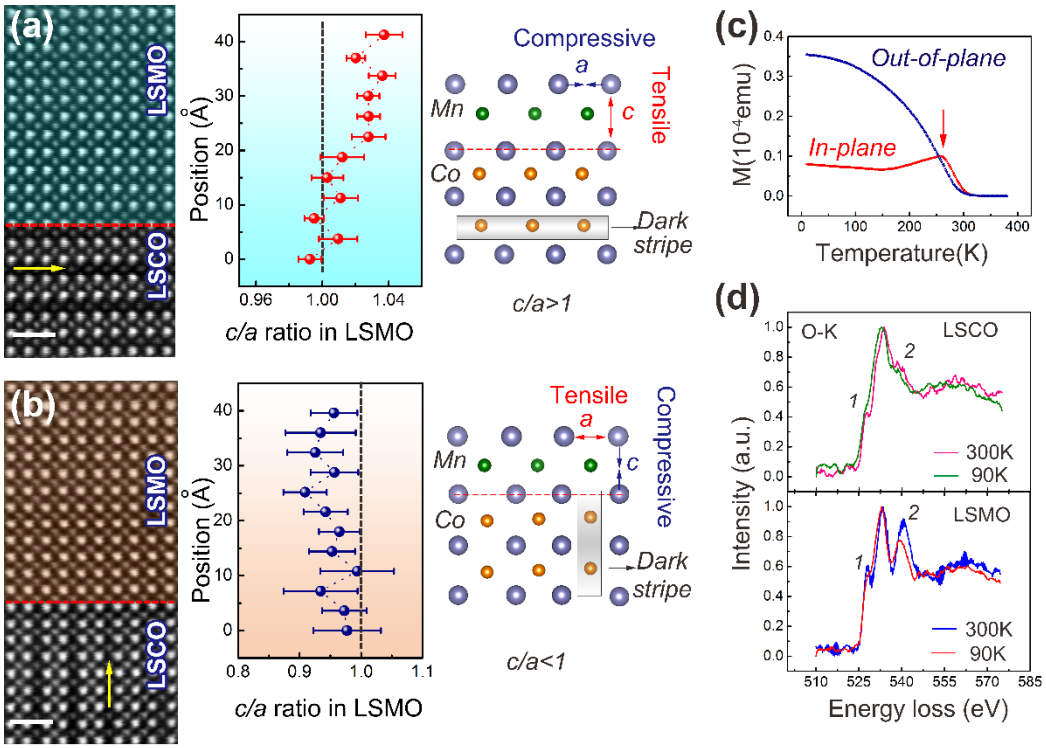

FIG. 5. (a) and (b) HAADF images with horizontal and vertical dark stripes in LSCO

layer as well as *c/a* ratios in LSMO along the *c* direction. The measurements started from LSCO/LSMO interface to the top of LSMO layer. The yellow arrows indicate the directions of the dark stripe. The corresponding schematic diagrams are inserted to show the strain effect from LSCO to LSMO, respectively. Red spheres are the *c/a* ratios in LSMO layer with the horizontal stripes in LSCO, blue spheres are the *c/a* ratios in LSMO layer with the vertical stripes in LSCO. The scale bar in (a) and (b) is 1 nm. (c) Thermomagnetic FC in-plane and out-of-plane curves of the LSCO/LSMO/LSCO, Sr = 0.5. The data were acquired with in-plane and out-of-plane applied field of 500 Oe, respectively. (d) EELS spectra of O K edge were taken from the LSCO/LSMO/LSCO sample at 300K and 90K, respectively. Top panel: O-K edge in LSCO; bottom panel: O-K edge in LSMO.

In addition, the MAE of the LSCO/LSMO/LSCO film is enhanced by two orders of magnitude compared with that in the bulk LSMO (see details in Supplementary Materials Fig. S3). To reveal the origin of the increase of MAE, we consider the phenomenological theory proposed by Bruno [53]. The general form of MAE (*G*) for a given crystalline structure can be expressed by spherical harmonics:

$$G_{cryst.}(\boldsymbol{\Omega_M}) = \sum_{l\ even} \sum_{m=-l}^{m=l} k_l^m(H_M) Y_l^m(\boldsymbol{\Omega_M}) \quad (1)$$

Where $\boldsymbol{\Omega_M}$ is the magnetization direction, H_M is the projection of the external field along the magnetization direction $\boldsymbol{\Omega_M}$; α_1, α_2, α_3 describe $\boldsymbol{\Omega_M}$ in the space coordinates system with $\alpha_1^2+\alpha_2^2+\alpha_3^2 = 1$. Considering the crystalline symmetry, the anisotropy energy can be understood from an expansion in terms of the magnetization direction

($\boldsymbol{\Omega_M}$) relative to the crystalline axes:

$$G_{cryst.}(\boldsymbol{\Omega_M}) = b_0(H_M) + \sum_{i,j} b_{ij}(H_M)\alpha_i\,\alpha_j + \sum_{i,j,k,l} b_{ijkl}(H_M)\alpha_i\alpha_j\,\alpha_k\alpha_l + \cdots \quad (2)$$

Where $b_{0,\,i,\,j,\,k,\,l}$ are coefficients. The crystalline symmetry imposes some relationships between the coefficients of given order in the expansion. For instance, in a cubic system, the terms of order 2 are forbidden and the first nonvanishing contribution to the crystalline anisotropy is the order 4. The usual expression for the anisotropy of the cubic system is shown in equation (3):

$$G_{cryst.}(\boldsymbol{\Omega_M}) = K_0 + K_1(\alpha_1^2\alpha_2^2 + \alpha_2^2\alpha_3^2 + \alpha_3^2\alpha_1^2) + K_2\alpha_1^2\alpha_2^2\alpha_3^2 + K_3(\alpha_1^2\alpha_2^2 + \alpha_2^2\alpha_3^2 + \alpha_3^2\alpha_1^2)^2 + \cdots \quad (3)$$

Where K_0, K_1, K_2… are anisotropy coefficients. According to the MAE calculation equations (1-3), it is clearly pointed out that the lower symmetry of the system the higher the MAE.

In LSMO film, considering the inhomogeneous strains from nanodomains in LSCO, the in-plane lattice parameters of LSMO should be unequal in both orthogonal directions. This lattice anisotropy effect on the thin film reduces the symmetry of LSMO. The EELS mapping result also indicates the symmetry breaking at the interface (see Supplemental Material Fig. S4 [43]). Based on the equations (1-3), for the lower symmetry system, the forbidden anisotropy coefficients in the equations will be present. Then they give additional contributions to the magnetic anisotropy, and result in a MAE enhancement.

V. CONCLUSIONS

We have explored the physical mechanism of a perpendicular magnetic anisotropy in the LSMO perovskite layer via nanostructure engineering of oxygen deficiency in LSCO. Our TEM results reveal that the nanodomains in LSCO layers provide different strains to LSMO layers at RT. These inhomogeneous strains lead to a disordered orbital occupancy state on Mn^{3+} ions at RT. The lattice spacing shrinking in LSCO at low temperature supplies a more in-plane compressive strain to LSMO, which causes $d_{3z^2-r^2}$ orbitals to be highly occupied. The out-of-plane orbital anisotropy reorients spin moment to the *c* axis via spin-orbit interaction in LSMO. Consequently, the magnetic easy axis is perpendicular to the interface. Due to the symmetry breaking induced by the nanodomains in LSCO through the interface, the magnetic anisotropy energy in LSMO is enhanced by orders of magnitude.

The present paper provides a strong experimental support for a picture for the microscopic origin of the out-of-plane MCA in the LSCO/LSMO/LSCO-STO thin films, which is of technological interest in the context of magnetic and magneto-optical data storage media. This paper may expand the controllable magnetic engineering in atomic-scale and artificial confinement in oxide spintronics.

ACKNOWLEDGMENTS

The authors would like to acknowledge financial support by the National Key Research Program of China (Grants No. 2017YFA0206200 and No. 2016YFA0300701), the National Natural Science Foundation of China (Grants No. 11574376, No. 11874413 and No. 11934017), and China Scholarship Council for support of W.W. to study abroad. X.S. is grateful for support from the Youth Innovation Promotion Association of Chinese Academy of Sciences (Grant No. 2019009). The electron microscopy work was carried out at Institute of Physics, Chinese Academy of Sciences and Brookhaven National Laboratory (BNL). The work

at BNL is sponsored by the US Department of Energy (DOE) Basic Energy Sciences (BES), by the Materials Sciences and Engineering under Contract No. DE-SC0012704, and by the DOE BES Early Career Award Program at BNL. It is also supported by the resources of the Center for Functional Nanomaterials at BNL.

REFERENCES

[1] H.Y. Hwang, Y. Iwasa, M. Kawasaki, B. Keimer, N. Nagaosa, Y. Tokura, Nature materials **11,** 103 (2012).
[2] A. Ohtomo, H. Hwang, Nature **427,** 423 (2004).
[3] J. Haeni, P. Irvin, W. Chang, R. Uecker, P. Reiche, Y. Li, S. Choudhury, W. Tian, M. Hawley, B. Craigo, Nature **430,** 758 (2004).
[4] M. Fäth, S. Freisem, A. Menovsky, Y. Tomioka, J. Aarts, J. Mydosh, Science **285,** 1540 (1999).
[5] Z. Liao, M. Huijben, Z. Zhong, N. Gauquelin, S. Macke, R. Green, S. Van Aert, J. Verbeeck, G. Van Tendeloo, K. Held, Nature materials **15,** 425 (2016).
[6] B. Rivas-Murias, I. Lucas, P. Jiménez-Cavero, C.s. Magén, L. Morellón, F. Rivadulla, Nano letters **16,** 1736 (2016).
[7] Y. Tokura, Y. Tomioka, J. Magn. Magn. Mater. **200,** 1 (1999).
[8] J.M. De Teresa, A. Barthélémy, A. Fert, J.P. Contour, R. Lyonnet, F. Montaigne, P. Seneor, A. Vaures, Phys. Rev. Lett. **82,** 4288 (1999).
[9] M. Bowen, M. Bibes, A. Barthélémy, J.-P. Contour, A. Anane, Y. Lemaıtre, A. Fert, Appl. Phys. Lett. **82,** 233 (2003).
[10] M. Bibes, J.E. Villegas, A. Barthelemy, Adv. Phys. **60,** 5 (2011).
[11] F. Tsui, M. Smoak, T. Nath, C. Eom, Appl. Phys. Lett. **76,** 2421 (2000).
[12] J. Zhang, Z. Zhong, X. Guan, X. Shen, J. Zhang, F. Han, H. Zhang, H. Zhang, X. Yan, Q. Zhang, Nature communications **9,** 1923 (2018).
[13] Y. Takamura, R. Chopdekar, E. Arenholz, Y. Suzuki, Appl. Phys. Lett. **92,** 162504 (2008).
[14] H. Fujishiro, M. Ikebe, Y. Konno, Journal of the Physical Society of Japan **67,** 1799 (1998).
[15] F.J.A. den Broeder, D. Kuiper, A.P. van de Mosselaer, W. Hoving, Phys. Rev. Lett. **60,** 2769 (1988).
[16] J. Langer, J.H. Dunn, A. Hahlin, O. Karis, R. Sellmann, D. Arvanitis, H. Maletta, Phys. Rev. B **66,** 172401 (2002).
[17] F. El Gabaly, S. Gallego, C. Munoz, L. Szunyogh, P. Weinberger, C. Klein, A.K. Schmid, K.F. McCarty, J. de la Figuera, Phys. Rev. Lett. **96,** 147202 (2006).
[18] P. Bruno, J.-P. Renard, Applied Physics A **49,** 499 (1989).
[19] J. Dorantes-Dávila, H. Dreyssé, G.M. Pastor, Phys. Rev. Lett. **91,** 197206 (2003).
[20] D. Weller, J. Stöhr, R. Nakajima, A. Carl, M.G. Samant, C. Chappert, R. Mégy, P. Beauvillain, P. Veillet, G.A. Held, Phys. Rev. Lett. **75,** 3752 (1995).
[21] G.H.O. Daalderop, P.J. Kelly, F.J.A. den Broeder, Phys. Rev. Lett. **68,** 682 (1992).
[22] T. Burkert, O. Eriksson, P. James, S.I. Simak, B. Johansson, L. Nordström, Phys.

Rev. B **69,** 104426 (2004).
[23] N. Nakajima, T. Koide, T. Shidara, H. Miyauchi, H. Fukutani, A. Fujimori, K. Iio, T. Katayama, M. Nývlt, Y. Suzuki, Phys. Rev. Lett. **81,** 5229 (1998).
[24] B. Ujfalussy, L. Szunyogh, P. Bruno, P. Weinberger, Phys. Rev. Lett. **77,** 1805 (1996).
[25] M. Izumi, Y. Ogimoto, T. Manako, M. Kawasaki, Y. Tokura, J. Phys. Soc. Jpn. **71,** 2621 (2002).
[26] L.F. Kourkoutis, J. Song, H. Hwang, D. Muller, Proceedings of the National Academy of Sciences **107,** 11682 (2010).
[27] X. Hong, A. Posadas, C. Ahn, Appl. Phys. Lett. **86,** 142501 (2005).
[28] W.S. Choi, J.-H. Kwon, H. Jeen, J.E. Hamann-Borrero, A. Radi, S. Macke, R. Sutarto, F. He, G.A. Sawatzky, V. Hinkov, Nano letters **12,** 4966 (2012).
[29] J.H. Kwon, W.S. Choi, Y.K. Kwon, R. Jung, J.M. Zuo, H.N. Lee, M. Kim, Chem. Mater. **26,** 2496 (2014).
[30] J. Gazquez, W. Luo, M.P. Oxley, M. Prange, M.A. Torija, M. Sharma, C. Leighton, S.T. Pantelides, S.J. Pennycook, M. Varela, Nano letters **11,** 973 (2011).
[31] N. Biškup, J. Salafranca, V. Mehta, M.P. Oxley, Y. Suzuki, S.J. Pennycook, S.T. Pantelides, M. Varela, Phys. Rev. Lett. **112,** 087202 (2014).
[32] J. Zhang, X. Chen, Q. Zhang, F. Han, J. Zhang, H. Zhang, H. Zhang, H. Huang, S. Qi, X. Yan, ACS applied materials & interfaces **10,** 40951 (2018).
[33] X. Rui and R.F. Klie, Appl. Phys. Lett. **114,** 233101 (2019).
[34] Y. Zhang, S. Li, C. Sun, W. Gao, Materials Science and Engineering: B **98,** 54 (2003).
[35] J.H. Jeon, J.H. Je, S.J.L. Kang, J. Am. Ceram. Soc. **81,** 624 (1998).
[36] S. Pennycook, Ultramicroscopy **30,** 58 (1989).
[37] T.L. Meyer, H. Jeen, X. Gao, J.R. Petrie, M.F. Chisholm, H.N. Lee, Advanced Electronic Materials **2,** 1500201 (2016).
[38] H. Jeen, W.S. Choi, M.D. Biegalski, C.M. Folkman, I.C. Tung, D.D. Fong, J.W. Freeland, D. Shin, H. Ohta, M.F. Chisholm, H.N. Lee, Nature Materials **12,** 1057 (2013).
[39] O.H. Hansteen, H. Fjellvåg, B.C. Hauback, J. Solid State Chem. **141,** 411 (1998).
[40] O.H. Hansteen, H. Fjellvåg, B.C. Hauback, Journal of Materials Chemistry **8,** 2081 (1998).
[41] M. Abbate, J.C. Fuggle, A. Fujimori, L.H. Tjeng, C.T. Chen, R. Potze, G.A. Sawatzky, H. Eisaki, S. Uchida, Phys. Rev. B **47,** 16124 (1993).
[42] Z. Wang, J. Yin, Philosophical Magazine B **77,** 49 (1998).
[43] See Supplemental Material at http://link.aps.org/supplemental/ 10.1103/ PhysRevB.101.024406 for EELS fitting spectra for Co $L_{3,2}$ peaks, M-T curve for x = 0.2, M(H) measurement and EELS spectrum images at LSMO/LSCO interface.
[44] Y. Konishi, Z. Fang, M. Izumi, T. Manako, M. Kasai, H. Kuwahara, M. Kawasaki, K. Terakura, Y. Tokura, J. Phys. Soc. Jpn. **68,** 3790 (1999).
[45] C. Aruta, G. Ghiringhelli, V. Bisogni, L. Braicovich, N.B. Brookes, A. Tebano, G. Balestrino, Phys. Rev. B **80,** 014431 (2009).
[46] D. Pesquera, G. Herranz, A. Barla, E. Pellegrin, F. Bondino, E. Magnano, F.

Sánchez, J. Fontcuberta, Nature Communications **3,** 1189 (2012).
[47] J. Zhang, W. Wang, J. Zhang, X. Chen, F. Han, H. Huang, H. Zhang, B. Shen, R. Yu, J. Sun, AIP Advances **9,** 035130 (2019).
[48] J.H. Song, J.H. Park, J.Y. Kim, B.G. Park, Y.H. Jeong, H.J. Noh, S.J. Oh, H.J. Lin, C.T. Chen, Physical Review B **72,** 060405 (2005).
[49] J. Stöhr, H.C. Siegmann, *Magnetism: From Fundamentals to Nanoscale Dynamics*, Springer, Berlin, Heidelberg, 2006.
[50] G. Shibata, M. Kitamura, M. Minohara, K. Yoshimatsu, T. Kadono, K. Ishigami, T. Harano, Y. Takahashi, S. Sakamoto, Y. Nonaka, K. Ikeda, Z. Chi, M. Furuse, S. Fuchino, M. Okano, J.-i. Fujihira, A. Uchida, K. Watanabe, H. Fujihira, S. Fujihira, A. Tanaka, H. Kumigashira, T. Koide, A. Fujimori, npj Quantum Materials **3,** 3 (2018).
[51] T. Yokoyama, D. Matsumura, K. Amemiya, S. Kitagawa, N. Suzuki, T. Ohta, Journal of Physics: Condensed Matter **15,** S537 (2003).
[52] J. Stöhr, J. Magn. Magn. Mater. **200,** 470 (1999).
[53] P. Bruno, *Magnetismus von Festkörpern und grenzflächen*, Lecture Notes Forschungszentrum Jülich, Jülich, Germany,1993.